Intensity–Duration–Frequency curves at the global scale

Laurent G. Courty[a,*], Robert L. Wilby[a], John K. Hillier[a], Louise J. Slater[b]

[a] *Department of Geography and Environment, Loughborough University, LE11 3TU, UK*
[b] *School of Geography and Environment, University of Oxford, OX1 3QY, UK*

Abstract

Intensity-Duration-Frequency (IDF) curves usefully quantify extreme precipitation over various durations and return periods for engineering design. Unfortunately, sparse, infrequent or short observations hinder the creation of robust IDF curves in many locations. This paper presents the first global, multi-temporal (1 to 360 h) dataset of Generalized Extreme Value (GEV) parameters at 31 km resolution dubbed PXR-2 (Parametrized eXtreme Rain). Using these data we generalize site-specific studies to show that that GEV parameters typically scale robustly with event duration ($r^2 > 0.88$). Thus, we propose a universal IDF formula that allows estimates of rainfall intensity for a continuous range of durations (PXR-4). This parameter scaling property opens the door to estimating sub-daily IDF from daily records. We evaluate this characteristic for selected global cities and a high-density rain gauge network in the United Kingdom. We find that intensities estimated with PXR-4 are within ±20 % of PXR-2 for durations ranging between 2 to 360 h. PXR is immediately usable by earth scientists studying global precipitation extremes as well as engineers designing infrastructure in data-scarce regions.

Keywords: Frequency analysis, precipitation, design rainfall, ERA5, reanalysis

*Corresponding author
Email address: `l.courty@lboro.ac.uk` (Laurent G. Courty)

1. Introduction

Historical precipitation records are widely employed by civil engineers to compute Intensity–Duration–Frequency (IDF) curves, which are essential for the design of infrastructure like highways (e.g. Brown et al., 2013; NYS DoT, 2018), urban drainage networks (e.g. Battaglia et al., 2003; Brown et al., 2013) and dams (e.g. NYS DoEC, 1989). Indeed, IDF curves are used to create synthetic rainfalls that permit the sizing of structures for a given return period, often required by local regulations.

However, not all countries have historical rain gauge records that are long or dense enough to compute reliable IDF curves (e.g. Lumbroso et al., 2011). The lack of observational data for IDF analysis is particularly true in continents such as Africa (van de Giesen et al., 2014) and Asia, where most of the world's urbanization is expected to take place over coming decades (UN DESA, 2018). As a result, much new infrastructure is being built in regions where the historical record of precipitation is scarce or uncertain, hindering adequate sizing of water-related works.

The first limitation of the observational data records is the scarcity of spatial coverage. The classical solution to this problem is to interpolate rainfall between weather stations. However, interpolation performs poorly in locations where pluviometers are sparse (e.g. Xu et al., 2015; Kumari et al., 2017). One more sophisticated approach consists of analyzing regional precipitation patterns to estimate local characteristics such as IDF curves at the location of interest (e.g. Roux and Desbordes, 1996; Fowler and Kilsby, 2003; Domínguez et al., 2018). Most recently, IDF curves have been derived over the continental U.S. (Ombadi et al., 2018) using the PERSIANN-CDR satellite-based precipitation dataset (Ashouri et al., 2015). However, a global, consistent IDF dataset is still lacking.

The increasing resolution and reliability of global or near-global gridded precipitation datasets represents a key opportunity to develop alternative approaches to tackle engineering challenges such as the correct sizing of flood infrastructure. Global gridded precipitation estimates are typically obtained by meteorological reanalysis (e.g. Gelaro et al., 2017; Uppala et al., 2005), where weather observations are assimilated by numerical weather prediction models. Advanced data fusion schemes have been developed by merging gauge-, satellite-, and reanalysis-based data to generate enhanced global precipitation estimates (e.g. Beck et al., 2018; Sun et al., 2018). Although global weather data products are widely employed by the earth science community, their use in engineering is still limited to applications such as wind power generation (e.g. Staffell and Pfenninger, 2016; Olauson, 2018) or drought monitoring (e.g. Hao et al., 2014). This paper is the first attempt to study global IDF relationships using gridded precipitation datasets, in an effort to help address the issue of precipitation data scarcity.

A second issue that is common with precipitation data is that of temporal resolution. In many cases, sub-daily IDF records are required for engineering uses because small catchments that are sensitive to brief rainfall events often require appropriate storm-water drainage structures. There have been recent efforts to compile high-resolution rainfall datasets (Blenkinsop et al., 2018), however the vast majority of historical precipitation data are still collected at a daily resolution in most parts of the world. Such low temporal resolution presents a major challenge for engineers designing urban water infrastructure, where catchments are commonly tens of hectares with lag times of less than an hour (Berne et al., 2004).

This temporal limitation might be overcome by using a temporal scaling property of IDF curves to estimate sub-daily IDF from daily precipitation. Extreme precipitation intensities for a given event duration d typically follow a Generalized Extreme Value (GEV) distribution, and it has been shown that the location and scale parameters of the GEV scale with d (e.g. Menabde et al., 1999; Bougadis and Adamows, 2006; Overeem et al., 2008; Veneziano and Furcolo, 2002). For instance, it has been demonstrated that the IDF characteristic of a given site could be described by a Gumbel distribution where the parameters follow a power law for durations between 30 min and 24 h (Menabde et al., 1999). However, those studies analyzed only a few sites: 2 in South Africa and

Australia (Menabde et al., 1999), 5 in Canada (Bougadis and Adamows, 2006), and 12 in the Netherlands (Overeem et al., 2008). So it has not been possible to determine whether this scaling property holds at a global scale. This would be of practical interest in many parts of the world where daily rainfall data are more widely available than sub-daily records.

This paper first uses the ERA5 reanalysis to generate global IDF relationships modelled with a GEV distribution, then investigates the extent to which these relationships scale with the event duration d at a global level. The analysis led to the creation of two datasets. The Parameterized eXtreme Rainfall–2 (PXR-2) dataset compiles the GEV parameters for 19 events durations spanning 1 h to 360 h, whereas the Parameterized eXtreme Rainfall–4 (PXR-4) represents the global distribution of the four parameters of a generalized IDF formula.

2. Methodology

2.1. Input data

Precipitation data were obtained from the ERA5 deterministic reanalysis (Hersbach and Dick, 2016; Copernicus Climate Change Service, 2018) at a spatial resolution of 0.25° (~31 km) and temporal resolution of 1 h. We chose the ERA5 dataset for its high spatial and temporal resolution, its performance (Beck et al., 2018), and its permissive usage license. We employ all the complete calendar years available at the time of writing (i.e. 1979–2018).

We use hourly rain gauge records from the MIDAS database of the UK Meteorological Office (Met Office, 2012) as a reference dataset for comparison with the reanalysis data. The original dataset contains 650 stations with variable record lengths. We use only the stations where geographical coordinates are provided. Following Blenkinsop et al. (2017), we keep only the observations that do not exceed by more than 20 % the 1 h and 24 h precipitation historical maxima for the UK, defined respectively as 92 mm and 279 mm by Met Office (2018). After this quality control, we omit the years with $< 90\,\%$ of observations remaining, and retain only those stations with $\geq 90\,\%$ of years remaining over the entire time period. This results in a subset of 35 stations for analysis (see Fig. S6 for their location).

2.2. Estimation of distribution parameters

The GEV distribution is widely used to represent Annual Maxima Series (AMS) (e.g. Fowler and Kilsby, 2003; Overeem et al., 2008; Papalexiou and Koutsoyiannis, 2013) with the Cumulative Distribution Function (CDF):

$$F(I) = \begin{cases} \exp\left[-\left(\dfrac{I-\mu}{\sigma}\right)^{1/\kappa}\right] & \text{if } \kappa \neq 0 \\ \exp\left[\exp\left(-\dfrac{I-\mu}{\sigma}\right)\right] & \text{if } \kappa = 0 \end{cases} \tag{1}$$

where I is the rainfall intensity, μ the location parameter, σ the scale parameter and κ the shape parameter. This formulation of the GEV implies that the distribution is bounded from below, corresponding to the Fréchet distribution, when $\kappa < 0$ (Hosking et al., 1985; Overeem et al., 2008); other authors use a formulation of Eq. 1 that implies the opposite sign of κ (e.g. Papalexiou and Koutsoyiannis, 2013; Ragulina and Reitan, 2017). When $\kappa = 0$, the GEV is the Gumbel distribution.

The estimation of κ is notoriously difficult due to its sensitivity to record length (Overeem et al., 2008; Papalexiou and Koutsoyiannis, 2013; Ragulina and Reitan, 2017). Indeed, it has been demonstrated that for sample sizes less than 50, using a two parameters Gumbel distribution results in a smaller error than the three parameter GEV (Lu and Stedinger, 1992). However, using $\kappa = 0$ could considerably underestimate the precipitation intensity, especially for long return periods (Koutsoyiannis, 2004a,b). This represents an important safety concern when designing engineering structures like dams.

On the other hand, studies have found that κ tends to -0.114 irrespective of geographical location (Papalexiou and Koutsoyiannis, 2013) and event duration d (Overeem et al., 2008). Considering the difficulty of robustly estimating κ, and that the value tends to -0.114 independently of duration or geographical location, we decide to globally set the GEV shape parameter to $\kappa = -0.114$.

The parameters of location (μ) and scale (σ) are estimated using the Probability-Weighted Moments (PWM) method (Hosking et al., 1985). The confidence intervals of the parameter estimates are obtained via bootstrapping with 1000 samples. We assess the goodness of fit of the distribution using the Filliben test (Wilks, 2011). This test is based on a Q-Q plot between the AMS and the quantile estimate ($\mathrm{mm\,h^{-1}}$, see Eq. 2). The probability of exceedance of the AMS is estimated with the Cunnane plotting position (Wilks, 2011), and the quantile estimate is calculated at the same return period. The Filliben test statistic consists of the Pearson's correlation coefficient r on that Q-Q plot. The critical value for the test is estimated using the formula given by Heo et al. (2008). If $r \geq r_{\mathrm{crit}}$, the null hypothesis that the AMS follows the GEV distribution cannot be rejected.

After fitting the GEV, intensity is estimated by the inverse of the CDF, also called the quantile function:

$$i(d,T) = \mu_d + \sigma_d y \tag{2}$$

where y is expressed relative to the return period T in years with $T = 1/(1-F)$:

$$y = \left\{1 - [-\ln(1-1/T)]^{\kappa}\right\}/\kappa \tag{3}$$

With $\kappa = -0.114$, the variance of the estimated rainfall intensity i can be obtained with the formula proposed by Lu and Stedinger (1992):

$$\mathrm{Var}(i) = \sigma^2(1.1412 + 0.8216y + 1.2546y^2)/n \tag{4}$$

where n is the length of the AMS in years. The confidence interval of the precipitation intensity I can then be estimated as:

$$I \in i \pm t^*_{n-2}\sqrt{\frac{\mathrm{Var}(i)}{n}} \tag{5}$$

where t^*_{n-2} is the quantile of the Student's t distribution with $n-2$ degrees of freedom. For a sample size of 40 years and a 95 % confidence interval, this value is 2.024.

2.3. Scaling of distribution parameters

To assess the scaling of the distribution parameters (μ, σ) relative to the event duration, we find the annual maxima for 19 event durations d by using a rolling mean. Window sizes are chosen to reflect a relatively regular spacing on a logarithmic scale and to present an equal number of durations for sub- and super-daily events. The selected sub- and super-daily durations are 1, 2, 3, 4, 6, 8, 10, 12, 18 and 24 h, and 1, 2, 3, 4, 5, 6, 8, 10, 12 and 15 days, respectively. Subsequently, the GEV parameters are estimated for each duration and ERA5 cell. Considering the spatial resolution of 0.25°, the 19 durations and the 1000 samples bootstrap, in total the GEV is fitted 1.97×10^{10} times to the AMS. Global maps of the estimated GEV parameters for each duration are compiled in the PXR-2 dataset (Courty et al., 2019), alongside their uncertainties.

Following Menabde et al. (1999), we assume that μ and σ scale with d according to a power law, but where they assert a single scaling gradient for both parameters we allow each to scale independently. This independent scaling of the two parameters appears typical for ERA5 data (Fig. S4 and S5). The scaling is therefore expressed as

$$\mu_d = ad^{\alpha} \qquad \sigma_d = bd^{\beta} \tag{6}$$

where d is the event duration in hours and a and α are the scaling parameters for μ, and b and β those for σ. These power-law relationships are straight lines in logarithmic space. For simplicity and ease of reproducibility (e.g. by practitioners) the scaling parameters are then estimated by Ordinary Least Squares (OLS) regression. Pearson's r^2 is used to test the linear relationship of the studied variables. The PXR-4 dataset (Courty et al., 2019) comprises the global distribution of these four parameters and their uncertainty.

Substituting μ_d and σ_d into Eq.2 with their scaled form from Eq. 6 we obtain a general IDF formula Eq. 7 that takes the parameters a, α and b, β specific to a given geographical location.

$$i(d, T) = ad^{\alpha} - bd^{\beta}y \tag{7}$$

3. Results

3.1. Global GEV parameters

The PXR-2 dataset comprises worldwide GEV parameters estimated from the ERA5 data for all 19 durations (1 h to 360 h), along with their uncertainties. This set of parameters is made freely available to accompany this paper (Courty et al., 2019).

The Filliben goodness of fit test indicates that at the 5 % significance level the null hypothesis that the annual maxima follow a GEV distribution with $\kappa = -0.114$ can be rejected in 5.7 % of the fitted cells (geographical location and duration). Considering the number of tests involved (19.7×10^6), $\approx$5 % of rejection is expected at the 5 % significance level (Bland and Altman, 1995). Here, the lower goodness of fit occurs in spatially coherent areas, located mostly in the drier regions of the Atlantic and Pacific oceans, the Sahara, the south of the Arabian peninsula, tropical Africa and the upper Amazon (see Fig. S1). Similar goodness of fit estimates are obtained with the Lilliefors test (see Fig. S2). The goodness of fit data are also included in the PXR dataset (Courty et al., 2019).

The GEV parameter maps shown in Fig. 1 clearly display regional rainfall patterns, such as tropical rainfall and monsoon (e.g. south Asia, Kripalani et al., 2007), orographic rainfall over mountainous regions (e.g. central Andes, Viale et al., 2011), and desert areas (e.g. Antartica, Vaughan et al., 1999).

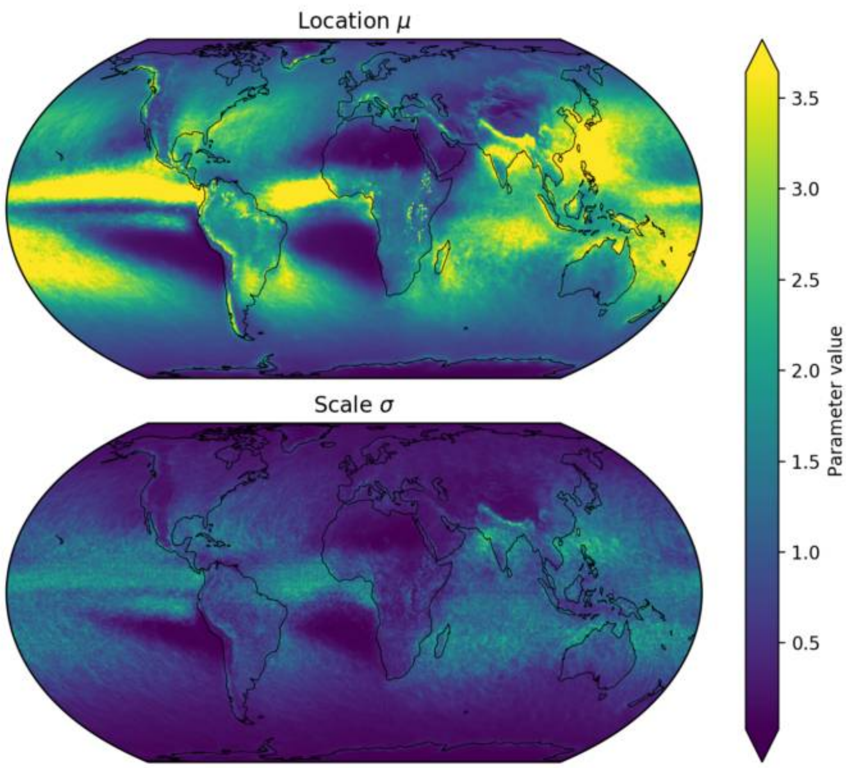

Figure 1: Global distribution of the GEV parameter values for an event duration of 24 h. Equivalent parameter values for event durations from 1 h to 360 h are available in the PXR-2 dataset (Courty et al., 2019).

3.2. Scaling of the GEV parameters

The fit of the relationship between μ or σ and d is quantified by calculating Pearson's r^2 for data presented on a log-log scale. In 99 % of the ERA5 cells r^2 exceeds 0.91 for μ and 0.88 for σ. Thus, the GEV parameters (μ, σ) both scale linearly on a log-log scale and this property appears to be robust and consistent at the global scale. The spatial distribution of r^2 values is also more consistent for μ than σ, with greater spatial variability for the latter (see Fig. S3).

The global distribution of the scaling gradients (α, β) is shown in Fig. 2. The spatial distribution of α seems to follow patterns with steeper gradients in deserts (e.g. Baja California, Patagonia, Sahara, Namib, Arabian peninsula, Taklamakan, Gobi) and smaller gradients in mountain ranges (e.g. Andes, Sierra Nevada, East African Rift, Scandes, Alps, Ural, Alborz, Caucasus, Himalaya, Kamchatka). β appears to follow similar patterns, but associated with a greater spatial variability than α.

Figure 3 illustrates how this scaling applies for selected global cities. The goodness of fit varies depending on the city, and the fitted regression lines tend to overestimate both GEV parameters at the shortest durations. Additionally, the scale parameter σ displays a weaker linear scaling and higher uncertainty than μ, a property that is in accordance with the r^2 values.

Figure 4 shows the differences between the parameter estimate (PXR-2) and its scaling (PXR-4) for both the whole world using ERA5, and at MIDAS rain gauges in the UK (see Section 2.1). In the case of the value of the whole world estimated from ERA5 (i.e. the PXR dataset), the application of the scaling relationship induces an overestimation of both μ and σ when $d < 3\,\mathrm{h}$, of μ when $d > 50\,\mathrm{h}$, and of σ when $d > 100\,\mathrm{h}$. When limited to the selected MIDAS gauges the differences for PXR follow the same shape. The differences due to scaling at the MIDAS stations are smaller when using the gauge data, especially for σ, and most notably for $d < 3\,\mathrm{h}$. Those differences in parameter estimates between PXR-2 and PXR-4 translate to the intensity estimates, with little variation due to the return period (see Fig. S7).

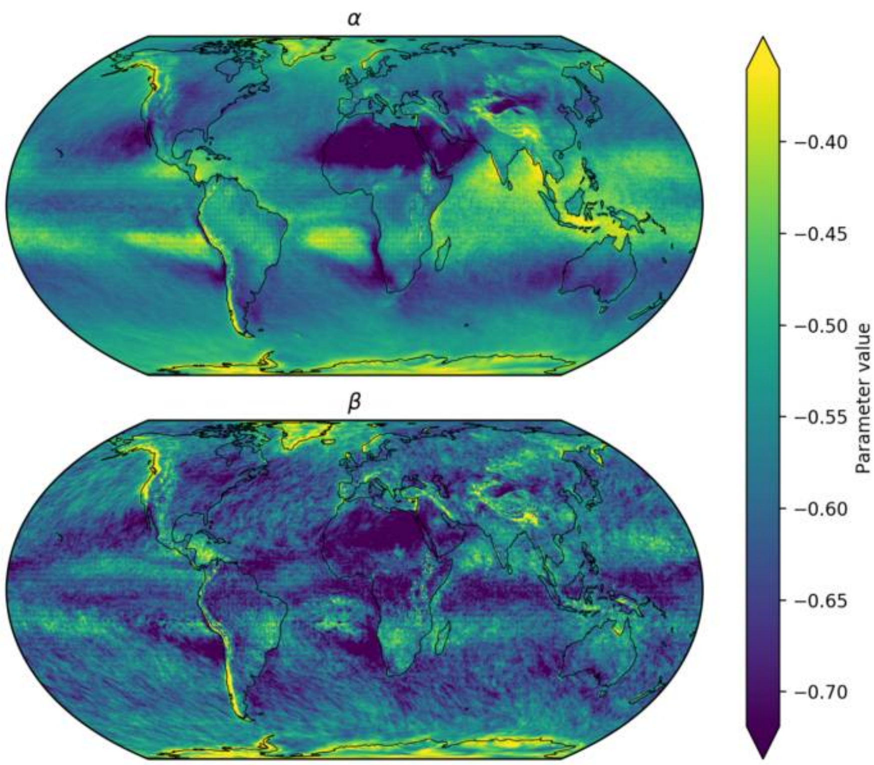

Figure 2: Global distribution of scaling gradients (α, β) of the respective GEV parameters (μ, σ). A smaller value indicates a steeper gradient.

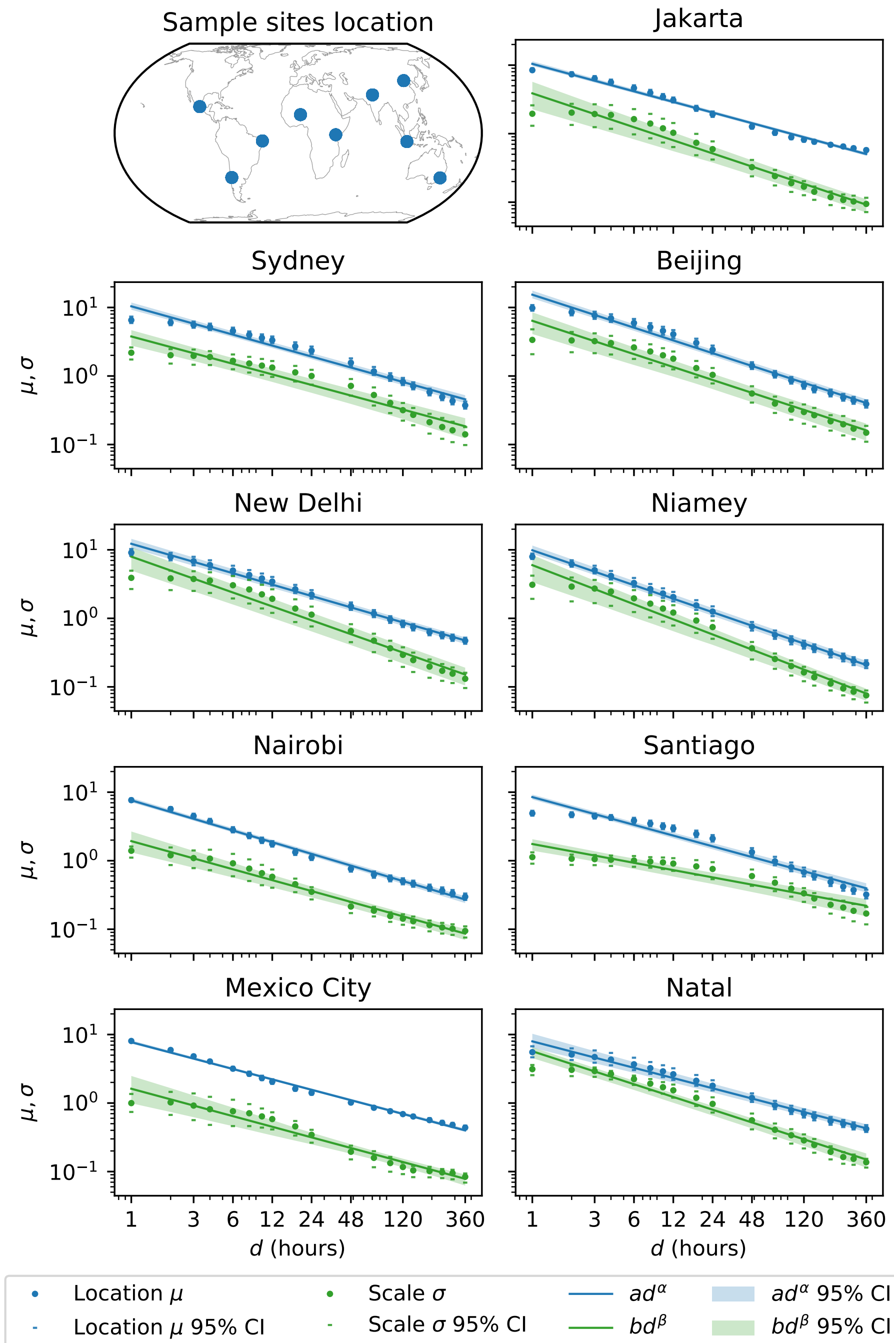

Figure 3: GEV parameter scaling for selected cities. Dots show the GEV parameters estimated for a given duration. The solid lines represent the parameter scaling property. Confidence intervals are obtained via the bootstrap method.

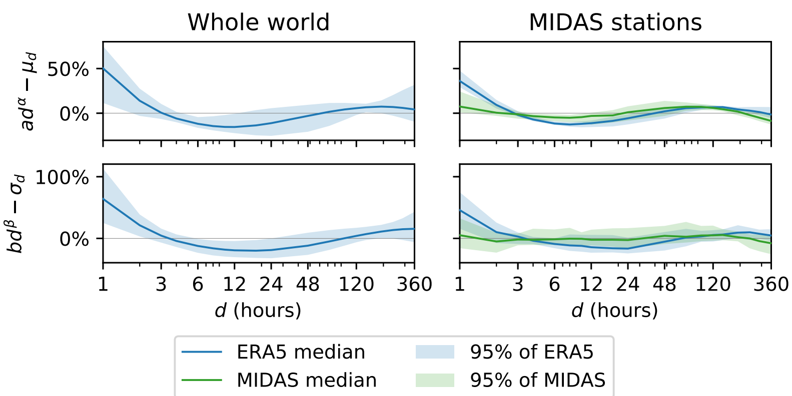

Figure 4: Median Percentage Error (MdPE) between the GEV parameters μ and σ estimated using the scaling parameters a, b, α and β and the actual μ_d and σ_d estimated by fitting the AMS. The greater the deviation from zero, the less accurate are α and β at estimating μ and σ. Values above zero indicate an overestimation of the GEV parameter.

4. Discussion

4.1. Global GEV parameters

Our analysis (Section 3.1, Fig. S1) concurs with previous work (e.g. Papalexiou and Koutsoyiannis, 2013) suggesting that the AMS of precipitation intensities are usefully described by a GEV distribution. However, using the newly-compiled PXR-2 dataset (Courty et al., 2019) we show this applies both on a global scale and with gridded precipitation data.

PXR provides a useful simplified description of global extreme precipitation. By describing the entire intensity–frequency distribution for a given d with only two parameters (i.e. not mean, median, mode, range etc.), more meaningful inter-comparison between areas is facilitated, as has been done in other fields in analogous situations (e.g. Hillier et al., 2013). The utility of PXR is enhanced by the relative ease with which the GEV parameters and their spatial distribution (e.g. Fig. 1) can be interpreted. Higher μ indicates greater typical precipitation intensities (i.e. the entire distribution becomes more intense), whilst higher σ values indicate more extreme events in the 'tail' of the distribution. Additionally, we showed in Section 3.1 that the parameter maps constituting PXR-2 represent qualitatively the expected geographical patterns of extreme precipitation, such as monsoon (e.g. south Asia, Kripalani et al., 2007), mountainous regions (e.g. central Andes, Viale et al., 2011), or desert areas (e.g. Antartica, Vaughan et al., 1999).

This dataset could have many hydrological applications ranging from engineering (e.g. Brown et al., 2013; NYS DoT, 2018) to extreme event studies (e.g. Lumbroso et al., 2011) and even broader applications such as landslide triggering (e.g. Postance et al., 2018) or global flood modelling (e.g. Trigg et al., 2016). Another possible application is the diagnostics of climate and weather models to assess their capacity to reflect the same scaling as those observed in nature.

Our results suggest that μ is broadly more robust than σ. Indeed, the estimates of σ reveal more variability than those of σ in both space (Fig. 1), duration (Fig. 3), and the scaling property (Fig. 2, 4, and S3). This higher variability of σ might be explained by the fact that the scale parameter is related to the intensity of less probable events (i.e. the tail of the probability density function). We acknowledge also that this work employs a relatively short AMS of 40 years that may well miss more extreme events. Indeed, using a longer series of annual maxima is key to improving estimates of GEV parameters (Papalexiou and Koutsoyiannis, 2013), although at the risk of overlooking the non-stationary nature of precipitation distributions (Westra et al., 2014).

4.2. Scaling in duration of the GEV parameters

Our study confirms that the GEV parameters μ and σ scale robustly with the duration d (e.g. Menabde et al., 1999; Overeem et al., 2008), and demonstrate that this relationship applies globally. However, in contrast to previous work there is strong evidence that μ and σ scale with different gradients (see Section 3.2). As a caveat, we note that the relationship between the parameters and d may be multi-scale (as denoted by breaks in slope of the log-log plots), and that more sophisticated scaling laws may be specified (Clauset et al., 2009). This multi-scaling property has been observed in a similar analysis of radar rainfall (Overeem et al., 2009), but is not obvious in previous work using gauges (Menabde et al., 1999; Overeem et al., 2008).

We suspect that the scaling differences between ERA5 and the rain gauges (see Fig. 4) are due to two main factors. First, the weather model used to generate ERA5 might underestimate the actual rainfall intensities of events of shorter durations, which are likely to be convective in nature and of limited spatial scale (Prein et al., 2015). Second, the actual scaling property of a gridded product might be inherently different to the scaling of precipitation measured at a point. Those differences in scaling might not be due to an inadequacy of the scaling hypothesis, but to an under-reporting of precipitation for events of $d < 3\,\mathrm{h}$ in the ERA5 dataset.

Therefore, in addition to providing sub-daily IDF information in parts of the world where no such data are readily available, PXR-4 also gives an insight about the feasibility of using daily rainfall records from pluviometers to estimate sub-daily IDF. Indeed, daily records are more common than data from automatic sub-daily gauges, and the lack of the latter is a challenge for engineers (e.g. Lumbroso et al., 2011). Additionally, the parsimonious representation in PXR-4 permits the generation of IDF curves for a continuous range of durations rather than discrete d in the case of PXR-2.

The PXR datasets represent areal precipitation which, as would be expected, results in lower intensities than gauges. For some applications an areal representation is actually preferred, as many hydrological processes of interest take place at the catchment scale. Decades of research have generated insights into the relationship between points and areal rainfall, and the estimation of the Areal Reduction Factor (ARF) (e.g. Rodriguez-Iturbe and Mejía, 1974; Asquith and Famiglietti, 2000; Kim et al., 2019). When comparing the IDF curves from PXR to those created with the MIDAS gauges (See Fig. 5), we note that the evolution of the Median Percentage Error (MdPE) in both duration and frequency is similar to the expected ARF, with the MdPE decreasing for longer d and shorter T (Pavlovic et al., 2016).

To illustrate the practical impacts of using PXR-4 or PXR-2, we compare the sizing of a culvert in an hypothetical 80 ha catchment in Jakarta with a time

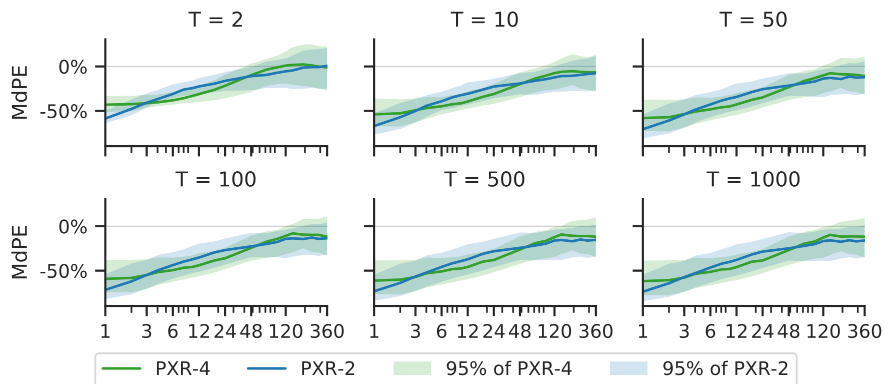

Figure 5: Median Percentage Error (MdPE) between precipitation intensities estimated from ERA5 and intensities obtained from MIDAS gauges. A negative error indicates that the intensity estimated from ERA5 is lower than that estimated from the MIDAS gauges.

of concentration $T_c = 2\,\text{h}$. Compared to the use of PXR-2, the use of PXR-4 results in an increase in the catchment outflow by 9.5 % for the 10-year rainfall and 14.4 % for the 100-year rainfall, which in turn induces a modification in the culvert sizing from 1 m to 1.2 m for the 10-year rainfall and 1.2 m to 1.5 m for the 100-year event. In this case, PXR-4 yields a more precautionary and potentially costly design than PXR-2. However, as discussed previously, more research is needed to identify whether those differences are the result of an underestimation of short rainfall intensities from ERA5, or an overestimation due to the scaling law used in PXR-4. For further information on this worked example, see the sizing calculations in Section S1.1 and the IDF curves for Jakarta from PXR-2 in Fig. S8.

5. Concluding remarks

Our results demonstrate the promising applicability of 1) reanalysis data to estimate IDF relationships, and 2) daily rainfall records to estimate sub-daily IDF curves. Our findings may be of notable interest for engineers working in data scarce regions and earth scientists interested in extreme precipitation variations. For durations between 2 h and 360 h, the precipitation intensities estimated from PXR-4 are within ±20 % of those estimated from PXR-2 (see Fig. S7).

More research is needed to study the actual range of validity of both PXR-2 and PXR-4 relative to catchment sizes and when compared to other options in data-scarce areas. The workflow used is adaptive enough to be employed with other gridded precipitation products. Future work might include the evaluation of the actual nature of the multi-scaling properties, including their physical causes, in both empirical observations and in climate model output.

Acknowledgments

This work is supported by the Natural Environment Research Council (NERC) via grant NE/R014361/1. The results are generated using Copernicus Climate Change Service information 2018. The accompanying PXR-2 and PXR-4 datasets are freely available online (Courty et al., 2019).

The Python programming language was used for the processing and plotting of the data, especially the modules xarray (Hoyer and Hamman, 2017), dask (Rocklin, 2015), pandas (McKinney, 2011), Numba (Lam et al., 2015), matplotlib (Hunter, 2007) and Cartopy (Met Office, 2010).

The world maps in this paper are drawn using the Equal Earth projection (Šavrič et al., 2019).

Authors contributions

All authors conceived the research idea, contributed to interpreting the results and writing the manuscript. Laurent Courty wrote the software, ran the analysis, and created the figures.

Competing interests

The authors declare no competing interests.

References

Ashouri H, Hsu KL, Sorooshian S, Braithwaite DK, Knapp KR, Cecil LD, Nelson BR, Prat OP. PERSIANN-CDR: Daily Precipitation Climate Data Record from Multisatellite Observations for Hydrological and Climate Studies. Bulletin of the American Meteorological Society 2015;96(1):69–83. URL: http://journals.ametsoc.org/doi/10.1175/BAMS-D-13-00068.1. doi:10.1175/BAMS-D-13-00068.1.

Asquith W, Famiglietti J. Precipitation areal-reduction factor estimation using an annual-maxima centered approach. Journal of Hydrology 2000;230(1-2):55–69. URL: https://www.sciencedirect.com/science/article/pii/S0022169400001700. doi:10.1016/S0022-1694(00)00170-0.

Battaglia P, Chocat B, Blanchard M, Others . La Ville et son assainissement. Certu, 2003.

Beck HE, Pan M, Roy T, Weedon GP, Pappenberger F, van Dijk AIJM, Huffman GJ, Adler RF, Wood EF. Daily evaluation of 26 precipitation datasets using Stage-IV gauge-radar data for the CONUS. Hydrology and Earth System Sciences Discussions 2018;:1–23URL: https://www.hydrol-earth-syst-sci-discuss.net/hess-2018-481/. doi:10.5194/hess-2018-481.

Berne A, Delrieu G, Creutin JD, Obled C. Temporal and spatial resolution of rainfall measurements required for urban hydrology. Journal of Hydrology 2004;299(3-4):166–79. URL: https://www.sciencedirect.com/science/article/pii/S0022169404003634. doi:10.1016/J.JHYDROL.2004.08.002.

Bland JM, Altman DG. Multiple significance tests: the Bonferroni method. BMJ (Clinical research ed) 1995;310(6973):170. URL: http://www.ncbi.nlm.nih.gov/pubmed/7833759http://www.pubmedcentral.nih.gov/articlerender.fcgi?artid=PMC2548561. doi:10.1136/BMJ.310.6973.170.

Blenkinsop S, Fowler HJ, Barbero R, Chan SC, Guerreiro SB, Kendon E, Lenderink G, Lewis E, Li XF, Westra S, Alexander L, Allan RP, Berg P, Dunn RJH, Ekström M, Evans JP, Holland G, Jones R, Kjellström E, Klein-Tank A, Lettenmaier D, Mishra V, Prein AF, Sheffield J, Tye MR. The INTENSE project: using observations and models to understand the past, present and future of sub-daily rainfall extremes. Advances in Science and Research 2018;15:117–26. URL: https://www.adv-sci-res.net/15/117/2018/. doi:10.5194/asr-15-117-2018.

Blenkinsop S, Lewis E, Chan SC, Fowler HJ. Quality-control of an hourly rainfall dataset and climatology of extremes for the UK. International Journal of Climatology 2017;37(2):722–40. URL: http://doi.wiley.com/10.1002/joc.4735. doi:10.1002/joc.4735.

Bougadis J, Adamows K. Scaling model of a rainfall intensity-duration-frequency relationship. Hydrological Processes 2006;(20):3747–57. doi:10.1002/hyp.6386.

Brown SA, Schall JD, Morris JL, Doherty CL, Stein SM, Warner JC. Urban Drainage Design Manual. Third edit ed.; volume 2009. National Highway Institute, 2013. URL: http://www.fhwa.dot.gov/engineering/hydraulics/library_arc.cfm?pub_number=22&id=140.

Chow VT. Open channel hydraulics. McGraw-Hill Book Company, Inc; New York, 1959.

Clauset A, Shalizi CR, Newman MEJ. Power-Law Distributions in Empirical Data. SIAM Review 2009;51(4):661–703. URL: http://epubs.siam.org/doi/10.1137/070710111. doi:10.1137/070710111.

Copernicus Climate Change Service . Climate Data Store. 2018. URL: https://cds.climate.copernicus.eu.

Courty LG, Wilby RL, Hillier JK, Slater LJ. Parametrized eXtreme Rainfall. 2019. doi:10.5281/zenodo.2616438.

Domínguez R, Carrizosa E, Fuentes GE, Arganis ML, Osnaya J, Galván-Torres AE. Análisis regional para estimar precipitaciones de diseño en la república mexicana. Tecnología y Ciencias del Agua 2018;9(1):05–29. doi:10.24850/j-tyca-2018-01-01.

Fowler HJ, Kilsby CG. A regional frequency analysis of United Kingdom extreme rainfall from 1961 to 2000. International Journal of Climatology 2003;23(11):1313–34. URL: http://doi.wiley.com/10.1002/joc.943. doi:10.1002/joc.943.

Gelaro R, McCarty W, Suárez MJ, Todling R, Molod A, Takacs L, Randles CA, Darmenov A, Bosilovich MG, Reichle R, Wargan K, Coy L, Cullather R, Draper C, Akella S, Buchard V, Conaty A, da Silva AM, Gu W, Kim GK, Koster R, Lucchesi R, Merkova D, Nielsen JE, Partyka G, Pawson S, Putman W, Rienecker M, Schubert SD, Sienkiewicz M, Zhao B, Gelaro R, McCarty W, Suárez MJ, Todling R, Molod A, Takacs L, Randles CA, Darmenov A, Bosilovich MG, Reichle R, Wargan K, Coy L, Cullather R, Draper C, Akella S, Buchard V, Conaty A, Silva AMd, Gu W, Kim GK, Koster R, Lucchesi R, Merkova D, Nielsen JE, Partyka G, Pawson S, Putman W, Rienecker M, Schubert SD, Sienkiewicz M, Zhao B. The Modern-Era Retrospective Analysis for Research and Applications, Version 2 (MERRA-2). Journal of Climate 2017;30(14):5419–54. URL: http://journals.ametsoc.org/doi/10.1175/JCLI-D-16-0758.1. doi:10.1175/JCLI-D-16-0758.1.

van de Giesen N, Hut R, Selker J. The Trans-African Hydro-Meteorological Observatory (TAHMO). Wiley Interdisciplinary Reviews: Water 2014;1(4):341–8. URL: http://doi.wiley.com/10.1002/wat2.1034. doi:10.1002/wat2.1034.

Hao Z, AghaKouchak A, Nakhjiri N, Farahmand A. Global integrated drought monitoring and prediction system. Scientific Data 2014;1:140001. URL: http://www.nature.com/articles/sdata20141. doi:10.1038/sdata.2014.1.

Heo JH, Kho YW, Shin H, Kim S, Kim T. Regression equations of probability plot correlation coefficient test statistics from several probability distributions. Journal of Hydrology 2008;355(1-4):1–15. URL: https://www.sciencedirect.com/science/article/pii/S0022169408000632. doi:10.1016/J.JHYDROL.2008.01.027.

Hersbach H, Dick L. ERA5 reanalysis is in production. ECMWF Newsletter 147 2016;(147):7. URL: http://www.ecmwf.int/sites/default/files/elibrary/2016/16299-newsletter-no147-spring-2016.pdf.

Hillier J, Smith M, Clark C, Stokes C, Spagnolo M. Subglacial bedforms reveal an exponential size–frequency distribution. Geomorphology 2013;190:82–91. URL: https://www.sciencedirect.com/science/article/pii/S0169555X13001049#! doi:10.1016/J.GEOMORPH.2013.02.017.

Hosking JRM, Wallis JR, Wood EF. Estimation of the Generalized Extreme-Value Distribution by the Method of Probability-Weighted Moments. Technometrics 1985;27(3):251–61. URL: http://www.tandfonline.com/doi/abs/10.1080/00401706.1985.10488049. doi:10.1080/00401706.1985.10488049.

Hoyer S, Hamman JJ. xarray: N-D labeled Arrays and Datasets in Python. Journal of Open Research Software 2017;5(1). URL: http://openresearchsoftware.metajnl.com/articles/10.5334/jors.148/. doi:10.5334/jors.148.

Hunter JD. Matplotlib: A 2D Graphics Environment. Computing in Science & Engineering 2007;9(3):90–5. URL: http://ieeexplore.ieee.org/document/4160265/. doi:10.1109/MCSE.2007.55.

Kim J, Lee J, Kim D, Kang B. The role of rainfall spatial variability in estimating areal reduction factors. Journal of Hydrology 2019;568:416–26. URL: https://www.sciencedirect.com/science/article/pii/S0022169418308692#f0030. doi:10.1016/j.jhydrol.2018.11.014.

Koutsoyiannis D. Statistics of extremes and estimation of extreme rainfall: I. Theoretical investigation / Statistiques de valeurs extrêmes et estimation de précipitations extrêmes: I. Recherche théorique. Hydrological Sciences Journal 2004a;49(4). URL: https://www.tandfonline.com/doi/full/10.1623/hysj.49.4.575.54430. doi:10.1623/hysj.49.4.575.54430.

Koutsoyiannis D. Statistics of extremes and estimation of extreme rainfall: II. Empirical investigation of long rainfall records. Hydrological Sciences Journal 2004b;49(4). URL: https://www.tandfonline.com/doi/full/10.1623/hysj.49.4.591.54424. doi:10.1623/hysj.49.4.591.54424.

Kripalani RH, Oh JH, Kulkarni A, Sabade SS, Chaudhari HS. South Asian summer monsoon precipitation variability: Coupled climate model simulations and projections under IPCC AR4. Theoretical and Applied Climatology 2007;90(3-4):133–59. URL: http://link.springer.com/10.1007/s00704-006-0282-0. doi:10.1007/s00704-006-0282-0.

Kumari M, Singh CK, Basistha A. Clustering Data and Incorporating Topographical Variables for Improving Spatial Interpolation of Rainfall in Mountainous Region. Water Resources Management 2017;31(1):425–42. URL: http://link.springer.com/10.1007/s11269-016-1534-0. doi:10.1007/s11269-016-1534-0.

Lam SK, Pitrou A, Seibert S. Numba: a LLVM-based Python JIT compiler. In: Proceedings of the Second Workshop on the LLVM Compiler Infrastructure in HPC - LLVM '15. New York, New York, USA: ACM Press; 2015. p. 1–6. URL: http://dl.acm.org/citation.cfm?doid=2833157.2833162. doi:10.1145/2833157.2833162.

Lu LH, Stedinger JR. Variance of two- and three-parameter GEV/PWM quantile estimators: formulae, confidence intervals, and a comparison. Journal of Hydrology 1992;138(1-2):247–67. URL: https://www.sciencedirect.com/science/article/pii/002216949290167T. doi:10.1016/0022-1694(92)90167-T.

Lumbroso D, Boyce S, Bast H, Walmsley N. The challenges of developing rainfall intensity-duration-frequency curves and national flood hazard maps for the Caribbean. Journal of Flood Risk Management 2011;4(1):42–52. URL: http://doi.wiley.com/10.1111/j.1753-318X.2010.01088.x. doi:10.1111/j.1753-318X.2010.01088.x.

McKinney W. pandas: a Foundational Python Library for Data Analysis and Statistics. In: Proceedings of the 1st Workshop on Python for High-Performance and Scientific Computing. 2011. .

Menabde M, Seed A, Pegram G. A simple scaling model for extreme rainfall. Water Resources Research 1999;35(1):335–9. URL: http://doi.wiley.com/10.1029/1998WR900012. doi:10.1029/1998WR900012.

Met Office . cartopy. 2010. URL: https://scitools.org.uk/cartopy.

Met Office . Met Office Integrated Data Archive System (MIDAS) Land and Marine Surface Stations Data (1853-current). 2012. URL: http://catalogue.ceda.ac.uk/uuid/220a65615218d5c9cc9e4785a3234bd0.

Met Office . UK climate - Extremes. 2018. URL: https://web.archive.org/web/20181206185424/https://www.metoffice.gov.uk/public/weather/climate-extremes/.

NYS DoEC . Guidelines for Design of Dams. Technical Report; New York State Department of Environmental Conservation; 1989.

NYS DoT . Highway drainage. In: Highway Design Manual. New York State Department of Transportation; volume 8; 2018. URL: https://www.dot.ny.gov/divisions/engineering/design/dqab/hdm/chapter-8.

Olauson J. ERA5: The new champion of wind power modelling? Renewable Energy 2018;126:322–31. URL: https://www.sciencedirect.com/science/article/pii/S0960148118303677#fig1. doi:10.1016/J.RENENE.2018.03.056.

Ombadi M, Nguyen P, Sorooshian S, Hsu Kl. Developing Intensity-Duration-Frequency (IDF) Curves from Satellite-based Precipitation: Methodology and Evaluation. Water Resources Research 2018;URL: http://doi.wiley.com/10.1029/2018WR022929. doi:10.1029/2018WR022929.

Overeem A, Buishand A, Holleman I. Rainfall depth-duration-frequency curves and their uncertainties. Journal of Hydrology 2008;348(1-2):124–34. doi:10.1016/j.jhydrol.2007.09.044.

Overeem A, Buishand TA, Holleman I. Extreme rainfall analysis and estimation of depth-duration-frequency curves using weather radar. Water Resources Research 2009;45(10):1–15. doi:10.1029/2009WR007869.

Papalexiou SM, Koutsoyiannis D. Battle of extreme value distributions: A global survey on extreme daily rainfall. Water Resources Research 2013;49(1):187–201. URL: http://doi.wiley.com/10.1029/2012WR012557. doi:10.1029/2012WR012557.

Pavlovic S, Perica S, St Laurent M, Mejía A. Intercomparison of selected fixed-area areal reduction factor methods. Journal of Hydrology 2016;537:419–30. URL: https://www.sciencedirect.com/science/article/pii/S0022169416301329#b0020. doi:10.1016/j.jhydrol.2016.03.027.

Postance B, Hillier J, Dijkstra T, Dixon N. Comparing threshold definition techniques for rainfall-induced landslides: A national assessment using radar rainfall. Earth Surface Processes and Landforms 2018;43(2):553–60. URL: http://doi.wiley.com/10.1002/esp.4202. doi:10.1002/esp.4202.

Prein AF, Langhans W, Fosser G, Ferrone A, Ban N, Goergen K, Keller M, Tölle M, Gutjahr O, Feser F, Brisson E, Kollet S, Schmidli J, van Lipzig NPM, Leung R. A review on regional convection-permitting climate modeling: Demonstrations, prospects, and challenges. Reviews of Geophysics 2015;53(2):323–61. URL: http://doi.wiley.com/10.1002/2014RG000475. doi:10.1002/2014RG000475.

Ragulina G, Reitan T. Generalized extreme value shape parameter and its nature for extreme precipitation using long time series and the Bayesian approach. Hydrological Sciences Journal 2017;62(6):863–79. URL: https://www.tandfonline.com/doi/full/10.1080/02626667.2016.1260134. doi:10.1080/02626667.2016.1260134.

Rocklin M. Dask: Parallel Computation with Blocked algorithms and Task Scheduling. In: Huff K, Bergstra J, editors. Proceedings of the 14th Python in Science Conference. 2015. p. 130–6.

Rodriguez-Iturbe I, Mejía JM. On the transformation of point rainfall to areal rainfall. Water Resources Research 1974;10(4):729–35. URL: http://doi.wiley.com/10.1029/WR010i004p00729. doi:10.1029/WR010i004p00729.

Roux C, Desbordes M. Rainfall-frequency curves with a recent urban dense rainfall measurement network. Atmospheric Research 1996;42(1-4):163–76. URL: https://www.sciencedirect.com/science/article/pii/0169809595000615. doi:10.1016/0169-8095(95)00061-5.

Šavrič B, Patterson T, Jenny B. The Equal Earth map projection. International Journal of Geographical Information Science 2019;33(3):454–65. URL: https://www.tandfonline.com/doi/full/10.1080/13658816.2018.1504949. doi:10.1080/13658816.2018.1504949.

Staffell I, Pfenninger S. Using bias-corrected reanalysis to simulate current and future wind power output. Energy 2016;114:1224–39. URL: https://www.sciencedirect.com/science/article/pii/S0360544216311811. doi:10.1016/J.ENERGY.2016.08.068.

Sun Q, Miao C, Duan Q, Ashouri H, Sorooshian S, Hsu KL. A Review of Global Precipitation Data Sets: Data Sources, Estimation, and Intercomparisons. Reviews of Geophysics 2018;56(1):79–107. URL: http://doi.wiley.com/10.1002/2017RG000574. doi:10.1002/2017RG000574.

Texas DoT . Hydraulic Design Manual, 2016.

Trigg MA, Birch CE, Neal JC, Bates PD, Smith A, Sampson CC, Yamazaki D, Hirabayashi Y, Pappenberger F, Dutra E, Ward PJ, Winsemius HC, Salamon P, Dottori F, Rudari R, Kappes MS, Simpson AL, Hadzilacos G, Fewtrell TJ. The credibility challenge for global fluvial flood risk analysis. Environmental Research Letters 2016;11(9):094014. URL: http://stacks.iop.org/1748-9326/11/i=9/a=094014?key=crossref.b898d75acc25c871d21b6be9b2ebcd65. doi:10.1088/1748-9326/11/9/094014.

UN DESA . 2018 Revision of World Urbanization Prospects. Technical Report; United Nations; 2018. URL: https://www.un.org/development/desa/publications/2018-revision-of-world-urbanization-prospects.html.

Uppala SM, Kållberg PW, Simmons AJ, Andrae U, Bechtold VDC, Fiorino M, Gibson JK, Haseler J, Hernandez A, Kelly GA, Li X, Onogi K, Saarinen S, Sokka N, Allan RP, Andersson E, Arpe K, Balmaseda MA, Beljaars ACM, Berg LVD, Bidlot J, Bormann N, Caires S, Chevallier F, Dethof A, Dragosavac M, Fisher M, Fuentes M, Hagemann S, Hólm E, Hoskins BJ, Isaksen L, Janssen PAEM, Jenne R, Mcnally AP, Mahfouf JF, Morcrette JJ, Rayner NA, Saunders RW, Simon P, Sterl A, Trenberth KE, Untch A, Vasiljevic D, Viterbo P, Woollen J. The ERA-40 re-analysis. Quarterly Journal of the Royal Meteorological Society 2005;131(612):2961–3012. URL: http://doi.wiley.com/10.1256/qj.04.176. doi:10.1256/qj.04.176.

Vaughan DG, Bamber JL, Giovinetto M, Russell J, Cooper APR, Vaughan DG, Bamber JL, Giovinetto M, Russell J, Cooper APR. Reassessment of Net Surface Mass Balance in Antarctica. Journal of Climate 1999;12(4):933–46. URL: http://journals.ametsoc.org/doi/abs/10.1175/1520-0442%281999%29012%3C0933%3ARONSMB%3E2.0.CO%3B2. doi:10.1175/1520-0442(1999)012<0933:RONSMB>2.0.CO;2.

Veneziano D, Furcolo P. Multifractality of rainfall and scaling of intensity-duration-frequency curves. Water Resources Research 2002;38(12):42–1. URL: http://doi.wiley.com/10.1029/2001WR000372. doi:10.1029/2001WR000372.

Viale M, Nuñez MN, Viale M, Nuñez MN. Climatology of Winter Orographic Precipitation over the Subtropical Central Andes and Associated Synoptic and Regional Characteristics. Journal of Hydrometeorology 2011;12(4):481–507. URL: http://journals.ametsoc.org/doi/abs/10.1175/2010JHM1284.1. doi:10.1175/2010JHM1284.1.

Westra S, Fowler HJ, Evans JP, Alexander LV, Berg P, Johnson F, Kendon EJ, Lenderink G, Roberts NM. Future changes to the intensity and frequency of short-duration extreme rainfall. Reviews of Geophysics 2014;52(3):522–55. URL: http://doi.wiley.com/10.1002/2014RG000464. doi:10.1002/2014RG000464.

Wilks D. Frequentist Statistical Inference. International Geophysics 2011;100:133–86. URL: https://www.sciencedirect.com/science/article/pii/B9780123850225000051. doi:10.1016/B978-0-12-385022-5.00005-1.

Xu W, Zou Y, Zhang G, Linderman M. A comparison among spatial interpolation techniques for daily rainfall data in Sichuan Province, China. International Journal of Climatology 2015;35(10):2898–907. URL: http://doi.wiley.com/10.1002/joc.4180. doi:10.1002/joc.4180.

S1. Supplementary material

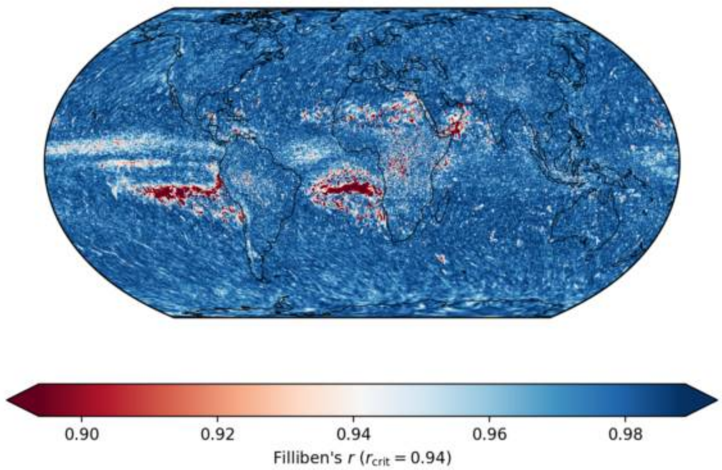

Figure S1: Global distribution of the mean of ~~the~~ Filliben's r along [across?] durations. The critical value r_{crit} at the 5 % significance level is calculated with the formula given by Heo et al. (2008). If $r > r_{\mathrm{crit}}$, the null hypothesis that the annual maxima follow the fitted GEV distribution cannot be rejected.

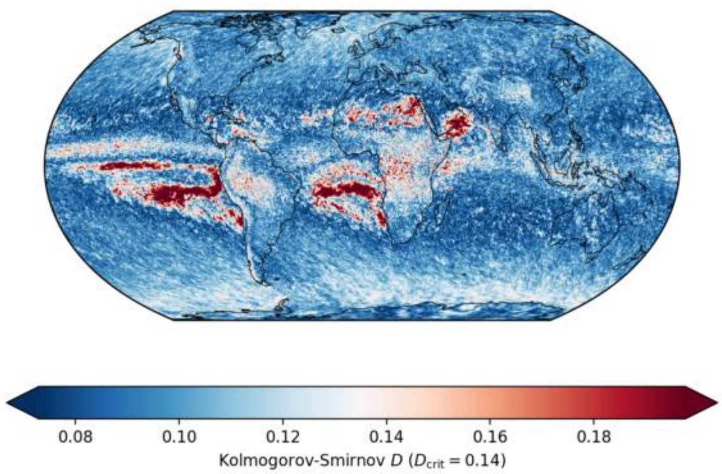

Figure S2: Global distribution of the mean of the Kolmogorov-Smirnov D along durations. The Lilliefors critical value D_{crit} at the 5 % significance level is estimated by Monte-Carlo simulation (Wilks, 2011). If $D < D_{\mathrm{crit}}$, the null hypothesis that the annual maxima follow the fitted GEV distribution cannot be rejected.

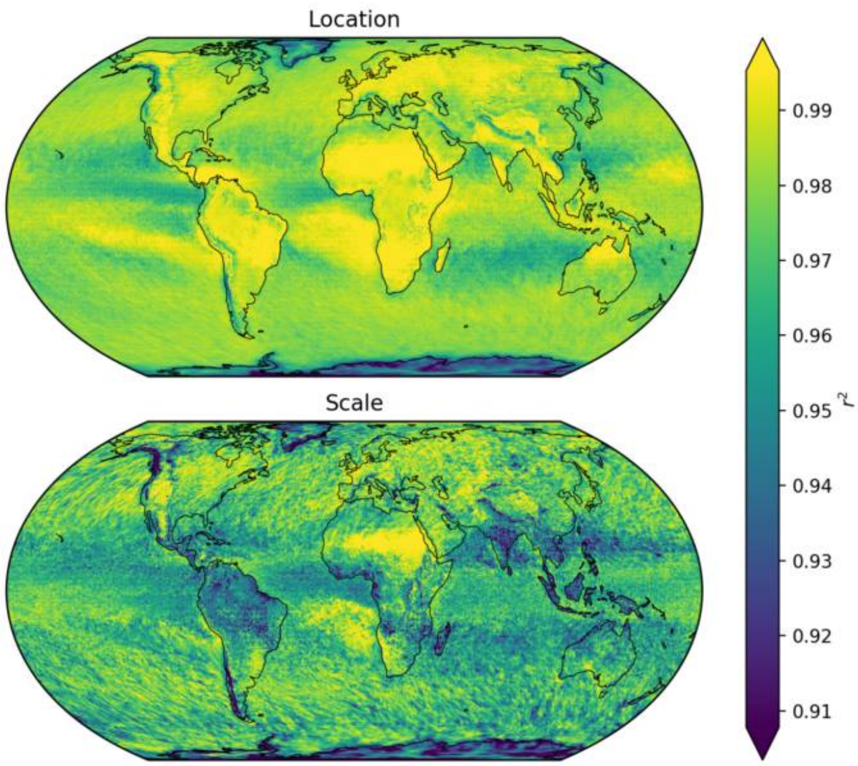

Figure S3: Global distribution of ~~the~~ Pearson's r^2 for the GEV parameters scaling across all durations. The higher the value, the better the fit of the regression line.

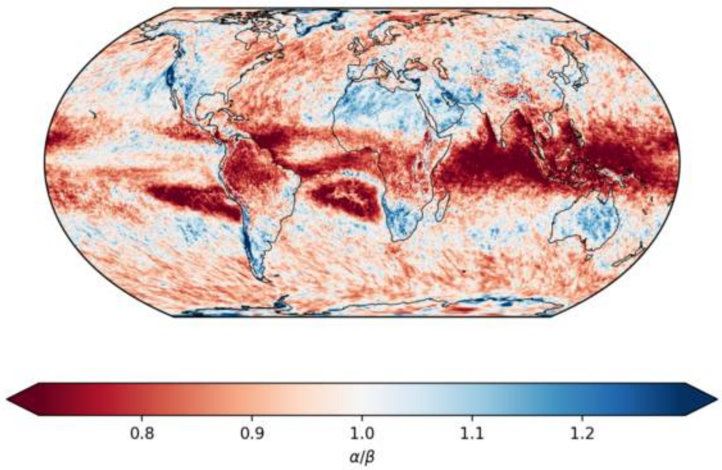

Figure S4: Ratio of the scaling gradients α and β. The more the value deviates from 1, the greater the difference between the scaling in duration of the parameters μ and σ

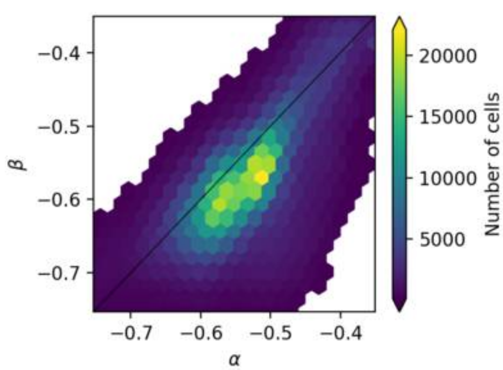

Figure S5: Relation between the scaling gradients α and β of the two GEV parameters location μ and scale σ. Bin size$<$ 100 are not shown.

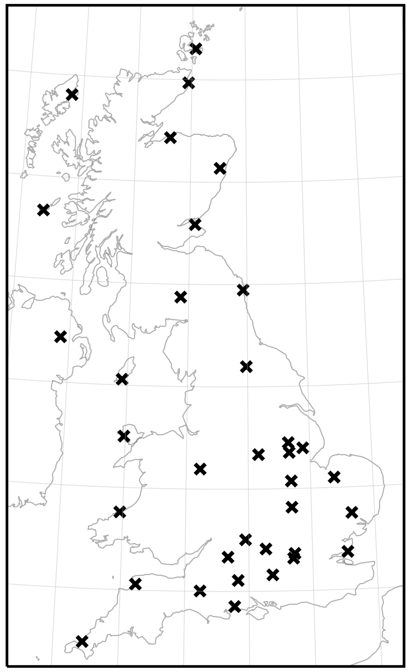

Figure S6: Location of the selected MIDAS rain gauges employed in the study.

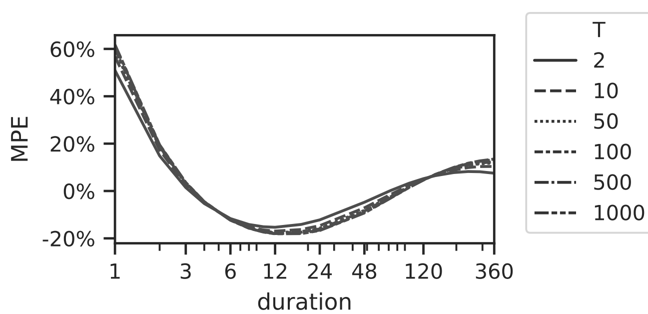

Figure S7: Mean Percentage Error between the intensities estimated from the scaled parameters (PXR-4) and the parameters estimated from the AMS at each duration (PXR-2). A positive value means that the intensity from PXR-4 is higher than the intensity from PXR-2.

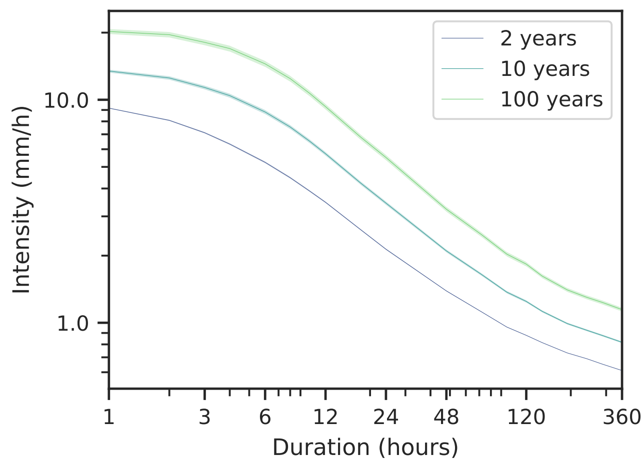

Figure S8: IDF curves for Jakarta obtained from PXR-2. The 95 % confidence interval is estimated using the method described in Lu and Stedinger (1992).

S1.1. Culvert sizing

We consider a catchment with characteristics as described in Table S1. We first estimate the rainfall intensity i by using Eq. 2 when using direct parameters or Eq. 7 when using scaled parameters.

Then we estimate the flow at the catchment outlet using the rational formula (Texas DoT, 2016)

$$Q = CiA_c/360 \tag{S1}$$

where Q is the peak flow in $\mathrm{m^3\,s^{-1}}$, C the runoff coefficient, i the rainfall intensity in $\mathrm{mm\,h^{-1}}$, and A_c the catchment surface area in ha. In the present case we consider an hypothetical catchment with an area of 80 ha, a runoff coefficient of 0.7 and a time of concentration T_c of 2 h (approximated with a combination of Kirpich and Kerby formulas). We therefore select a 2 h rainfall. The culvert is designed as a circular pipe with a slope S of $5\,\mathrm{mm\,m^{-1}}$ and a Manning's n of $0.012\,\mathrm{s\,m^{-1/3}}$. The pipe is sized as the standard diameter able to transit the flow Q when 90 % full. The culvert capacity is estimated with the

Gauckler–Manning–Strickler (GMS) formula (Chow, 1959):

$$Q = A_f \frac{1}{n} (\frac{A_f}{P})^{2/3} S^{1/2} \tag{S2}$$

where A_f is the flow area (m^2), P the wetted perimeter (m), and n the Manning's n ($\mathrm{s\,m^{-1/3}}$). We consider that the slope S is parallel to the pipe invert. In the case of a partially filled circular pipe, A_f and P are calculated using Eq. S3

$$P = \theta\phi \tag{S3a}$$

$$A_f = \frac{1}{8}(\theta - \sin\theta)\phi^2 \tag{S3b}$$

$$\theta = \arccos(1 - \frac{h}{\phi/2}) \tag{S3c}$$

where ϕ is the pipe internal diameter and h the water depth in the pipe.

We do the sizing with two return periods: 10 years and 100 years. We also compare the results obtained with the GEV parameters obtained via direct fitting versus those obtained by using the scaling relationship.

Table S1: Parameters for culvert sizing at the outlet of an hypothetical catchment in Jakarta. Runoff coefficient C and surface area A_c are hypotheticals. μ_{2h} and σ_{2h} are obtained from direct fitting. μ'_{2h} and σ'_{2h} are obtained by applying the scaling formula. The 95 % confidence interval is estimated with the bootstrap method.

Parameter	Value	Parameter	Value
A_c	80 ha	a	10.43 (9.72–11.40)
C	0.7	b	3.97 (2.26–5.72)
d	2 h	α	−0.51 (−0.53–−0.50)
T	10 & 100 years	β	−0.64 (−0.70–−0.54)
μ_{2h}	7.32 (6.93–7.89)	μ'_{2h}	7.30 (6.79–8.25)
σ_{2h}	2.03 (1.34–2.72)	σ'_{2h}	2.50 (1.53–3.54)

Table S2: Impact of the scaling hypothesis on the sizing of a circular culvert on an hypothetical catchment in Jakarta. The 95 % confidence interval is estimated with the method described in Lu and Stedinger (1992).

	μ_d, σ_d	ad^{α}, bd^{β}
T10 Rainfall ($\mathrm{mm\,h^{-1}}$)	12.5 (11.3–13.8)	13.7 (12.5–15.0)
T10 Outflow ($\mathrm{m^3\,s^{-1}}$)	1.9 (1.8–2.1)	2.1 (1.9–2.3)
T10 Pipe diameter (m)	1.0	1.2
T100 Rainfall ($\mathrm{mm\,h^{-1}}$)	19.6 (16.9–22.3)	22.4 (19.8–25.1)
T100 Outflow ($\mathrm{m^3\,s^{-1}}$)	3.0 (2.6–3.5)	4.5 (3.1–3.9)
T100 Pipe diameter (m)	1.2	1.5